Acta Astronautica 213 (2023) 792–804

Contents lists available at ScienceDirect

Acta Astronautica

journal homepage: www.elsevier.com/locate/actaastro

Mars orbit injection via aerocapture and low-thrust nonlinear orbit control

Edoardo Fornari [a], Mauro Pontani [b,*]

[a] Faculty of Civil and Industrial Engineering, Sapienza Università di Roma, Rome, Italy
[b] Department of Astronautical, Electrical, and Energy Engineering, Sapienza Università di Roma, Rome, Italy

ARTICLE INFO

Keywords:
Mars missions
Aerocapture
Low-thrust space trajectories
Nonlinear orbit control
Mars orbit injection

ABSTRACT

This research proposes a new strategy for Mars orbit injection, based on aerocapture and low-thrust nonlinear orbit control. The range of periapse altitudes that allow aerocapture is identified as a function of the hyperbolic excess velocity at Mars arrival, with reference to a large variety of atmospheric density profiles and different ballistic coefficients. This analysis proves that a safe periares altitudinal range leading to aerocapture in all atmospheric conditions does not exist. Three different correction maneuvers, aimed at avoiding both impact and escape, are identified. After the atmospheric arc, the spacecraft orbit exhibits large dispersions in terms of orbit elements. Therefore, the identification of an effective autonomous guidance strategy, capable of driving the spacecraft toward the desired operational orbit, is mandatory. To do this, low-thrust nonlinear orbit control is proposed as an effective option. A feedback law for the low-thrust direction and magnitude, with saturation of the thrust magnitude, is defined, and is proven to enjoy global stability properties. As a result, the spacecraft travels toward the operational orbit of interest, i.e. either (a) an areostationary orbit, (b) a quasi-synchronous inclined orbit, or (c) a low-altitude, sunsynchronous orbit. Monte Carlo simulations, with stochastic density profiles and uncertain initial conditions, point out that the strategy at hand is successful and allows reducing the overall propellant budget in comparison to direct orbit injection based on chemical propulsion. Moreover, the overall time of flight typically ranges from 45 to 140 days, and therefore it is much shorter than that required with the use of aerobraking. As a last advantage, low-thrust nonlinear orbit control allows achievement of a variety of operational orbits, with great accuracy.

1. Introduction

Several types of orbit injection maneuvers were used in past missions to Mars, including long-duration, multiple aerobraking passes, aimed at selecting the desired operational orbit. Planetary aerobraking consists of several atmospheric passes, which reduce the semimajor axis and eccentricity of the initial elliptic orbit about the planet of interest. It was investigated and performed in the context of the Mars Global Surveyor, Mars Odissey, and Mars Reconnaissance missions. Planetary aerocapture is a different technique and consists of a single atmospheric pass that reduces the hyperbolic velocity of a spacecraft (at planet arrival) to a value corresponding to an elliptic orbit. This kind of maneuver has been a subject of great interest in astrodynamics since the 1960's. The first work on aerocapture was done by Finch [1], Repic et al. [2], French and Cruz [3], Mease et al. [4], Walberg [5], Fuhry [6], and Brans and Fuhry [7]. Then Calise [8], Powell et al. [9], and Wercinski and Lyne [10] investigated the same problem, focusing on aerocapture trajectory and guidance. Most recently, Vinh et al. [11] analyzed aerocapture trajectories based upon bank modulation, whereas Kumar and Tewari [12,13] treated the overall spacecraft dynamics (trajectory and attitude) during aerocapture and aerobraking. Further recent studies on aerocapture are due to Heidric et al. [14], Albert et al. [15], and Roelke and Braun [16]. Closely related to aerocapture, Pontani and Teofilatto [17] focused on the identification of frozen, repeating-ground-track orbits after aerocapture at Mars.

This research proposes a new strategy for Mars orbit injection, based on aerocapture and low-thrust nonlinear orbit control. The range of periapse altitudes that allow aerocapture are identified as a function of the hyperbolic excess velocity at Mars arrival, with reference to a large variety of atmospheric density profiles. This preliminary analysis regards different spacecraft, with distinct ballistic coefficients, and aims to identify safe aerocapture corridors, even in the presence of different (and uncertain) density profiles. Then, suitable correction maneuvers, aimed at avoiding both impact and escape, are investigated. After the atmospheric arc, the spacecraft orbit exhibits large dispersions in terms of orbit elements. Therefore, the identification of an effective

* Corresponding author.
E-mail addresses: fornari.1695281@studenti.uniroma1.it (E. Fornari), mauro.pontani@uniroma1.it (M. Pontani).

https://doi.org/10.1016/j.actaastro.2023.07.025
Received 26 February 2023; Received in revised form 15 July 2023; Accepted 22 July 2023
Available online 25 July 2023

autonomous guidance strategy, capable of driving the spacecraft toward the desired operational orbit, is mandatory. To do this, low-thrust nonlinear orbit control is proposed as an effective option. Three different operational orbits are considered: (a) areostationary orbit, (b) quasi-synchronous, circular, inclined orbit, and (c) low-altitude, circular, sunsynchronous orbit. Monte Carlo simulations, with stochastic density profiles, different ballistic coefficient, and uncertain initial conditions, are performed, for the purpose of showing effectiveness and efficiency (in terms of propellant consumption) of the orbit injection strategy based on aerocapture and low-thrust nonlinear orbit control.

2. Orbit dynamics using modified equinoctial elements

This section is concerned with orbit dynamics of the space vehicle directed toward Mars and modeled as a point mass, in the context of a 3-degree-of-freedom problem. Orbital motion is modeled in the dynamical framework of the perturbed two-body problem, with the use of modified equinoctial elements (MEE).

2.1. Reference frames

As a preliminary step, the Mars-centered inertial (MCI) frame is introduced. It is associated with the right-hand sequence of unit vectors $(\hat{c}_1, \hat{c}_2, \hat{c}_3)$, where $(\hat{c}_1, \hat{c}_2)$ identifies the equatorial plane, $\hat{c}_1$ is aligned with the intersection of the equatorial plane and the fundamental plane of the ICRF/J2000 system (with positive component along the ascending node of the orbit of Mars), and $\hat{c}_3$ points along the Martian rotation axis. Two other useful frames (rotating together with the spacecraft) are the local horizontal (LH) frame, associated with $(\hat{r}, \hat{E}, \hat{N})$, and the local vertical local horizontal (LVLH) frame aligned with $(\hat{r}, \hat{\theta}, \hat{h})$. Unit vector $\hat{r}$ is directed along the instantaneous position vector $\underset{\rightarrow}{\mathbf{r}}$ (taken from Mars' center), $\hat{E}$ and $\hat{N}$ are aligned with the local East and North directions, respectively, whereas $\hat{h}$ points along the spacecraft angular momentum. Angles ξ (absolute longitude), φ (latitude), and ζ (heading) relate the MCI-frame to the LH-frame and to the LVLH-frame,

$$\begin{aligned}&[\hat{r} \quad \hat{\theta} \quad \hat{h}]^T = \mathbf{R}_1(\zeta)[\hat{r} \quad \hat{E} \quad \hat{N}]^T \\ &= \mathbf{R}_1(\zeta)\mathbf{R}_2(-\varphi)\mathbf{R}_3(\xi)[\hat{c}_1 \quad \hat{c}_2 \quad \hat{c}_3]^T\end{aligned} \tag{1}$$

where $\mathbf{R}_j(\chi)$ denotes the matrix associated with the elementary counterclockwise rotation by angle χ about axis j. Moreover, an additional relation between the ECI-frame and the LVLH-frame can be written in terms of orbit elements [18],

$$[\hat{r} \quad \hat{\theta} \quad \hat{h}]^T = \mathbf{R}_3(\omega + f)\mathbf{R}_1(i)\mathbf{R}_3(\Omega)[\hat{c}_1 \quad \hat{c}_2 \quad \hat{c}_3]^T \tag{2}$$

where Ω, ω, and f are respectively the right ascension of the ascending node (RAAN), argument of periapse, and true anomaly [18].

2.2. Orbit dynamics equations

The spacecraft dynamics can be described in terms of either spherical coordinates or osculating orbit elements, i.e. semimajor axis a, eccentricity e, inclination i, RAAN Ω, argument of periapse ω, and true anomaly f. However, the Gauss equations [18,19], which govern the time evolution of the orbit elements, become singular in the presence of a circular or equatorial orbit (and also when an elliptic orbit transitions to a hyperbola). For these reasons, the modified equinoctial elements [20] l, m, n, s, and q are chosen, in conjunction with the semilatus rectum (parameter) p, used in place of a. The five elements l, m, n, s, and q are defined as [20]

$$\begin{aligned}&l = e\cos(\Omega+\omega) \quad m = e\sin(\Omega+\omega) \\ &n = \tan\frac{i}{2}\cos\Omega \quad s = \tan\frac{i}{2}\sin\Omega \quad q = \Omega + \omega + f\end{aligned} \tag{3}$$

These are nonsingular for all Keplerian trajectories, except for equatorial retrograde orbits ($i = \pi$). If $\eta := 1 + l\cos q + m\sin q$, the instantaneous radius $r = \left|\underset{\rightarrow}{\mathbf{r}}\right|$ is $r = p/\eta$. Letting $x_6 \equiv q$ and $z := [x_1 \quad x_2 \quad x_3 \quad x_4 \quad x_5]^T \equiv [p \quad l \quad m \quad n \quad s]^T$, the governing equations can be written as

$$\dot{z} = \mathbf{G}(z, x_6)\boldsymbol{a} \tag{4}$$

$$\dot{x}_6 = \sqrt{\frac{\mu_M}{x_1^3}}\eta^2 + \sqrt{\frac{x_1}{\mu_M}}\,\frac{x_4\sin x_6 - x_5\cos x_6}{\eta}a_h \tag{5}$$

where μ_M is the Martian gravitational parameter, and

$$\mathbf{G}(z, x_6) = \sqrt{\frac{x_1}{\mu_M}}\begin{bmatrix} 0 & \frac{2x_1}{\eta} & 0 \\ \mathrm{s}_{x_6} & \frac{(\eta+1)\mathrm{c}_{x_6} + x_2}{\eta} & -\frac{x_4\mathrm{s}_{x_6} - x_5\mathrm{c}_{x_6}}{\eta}x_3 \\ -\mathrm{c}_{x_6} & \frac{(\eta+1)\mathrm{s}_{x_6} + x_3}{\eta} & \frac{x_4\mathrm{s}_{x_6} - x_5\mathrm{c}_{x_6}}{\eta}x_2 \\ 0 & 0 & \frac{1+x_4^2+x_5^2}{2\eta}\mathrm{c}_{x_6} \\ 0 & 0 & \frac{1+x_4^2+x_5^2}{2\eta}\mathrm{s}_{x_6} \end{bmatrix} \tag{6}$$

with $\mathrm{s}_\vartheta := \sin\vartheta$ and $\mathrm{c}_\vartheta := \cos\vartheta$ (ϑ denotes a generic angle). The (3×1)-vector $\boldsymbol{a}$ collects the components (in the LVLH-frame) of the non-Keplerian acceleration that affects the spacecraft motion. These are denoted with (a_r, a_θ, a_h). Vector $\boldsymbol{a}$ includes both the thrust acceleration and the perturbing acceleration inherent to the space environment. It is convenient to distinguish these two contributions, thus $\boldsymbol{a} = \boldsymbol{a}_T + \boldsymbol{a}_P$, where subscripts T and P refer to thrust and perturbations, respectively.

Let T_{max} and m_0 represent the maximum available thrust magnitude and the initial mass. If x_7 denotes the mass ratio and T the thrust magnitude, for x_7 the following equation can be obtained:

$$\dot{x}_7 := \frac{\dot{m}}{m_0} = -\frac{u_T}{c} \tag{7}$$

with $0 \le u_T \le u_T^{(max)}$, whereas $u_T := (T/m_0)$ and $u_T^{(max)} := (T_{max}/m_0)$. Symbol c represents the (constant) effective exhaust velocity of the low-thrust propulsion system. The magnitude of the instantaneous thrust acceleration is $a_T = u_T m_0/m = u_T/x_7$ and is constrained to the $0 \le a_T \le a_T^{(max)}$, where $a_T^{(max)} = u_T^{(max)}/x_7$. Moreover, the thrust acceleration can be expressed as $\boldsymbol{a}_T = \boldsymbol{u}_T/x_7$, where $\boldsymbol{u}_T$ has magnitude constrained to $[0, u_T^{(max)}]$.

In conclusion, the spacecraft dynamics are described in terms of the state vector $\boldsymbol{x} := [z^T \quad x_6 \quad x_7]^T = [x_1 \quad x_2 \quad x_3 \quad x_4 \quad x_5 \quad x_6 \quad x_7]^T$, whereas the control vector is $\boldsymbol{u}_T$, directly related to the thrust acceleration. Equations (4), (5) and (7) represent the governing equations.

3. Dynamical environment

While orbiting Mars, the space vehicle is affected mainly by its gravitational field, and its orbital motion can be appropriately investigated by employing a perturbed two-body-problem model. As a first perturbing action, the Martian gravitational potential differs to some extent from that generated by a spherical mass distribution. As a result, some significant harmonics of areopotential are to be included in the dynamical model, in order to yield more realistic results from simulations. Other than Martian asphericity, the third-body perturbation due to the gravitational attraction of the Sun represents an additional contribution. Moreover, for spacecraft that reach low altitudes, the drag perturbing acceleration plays a role as well. Lastly, also the perturbing effects due to solar radiation pressure are nonnegligible. This section

describes and models all these perturbations.

3.1. Harmonics of the areopotential

This study employs the Goddard Mars Model-3 (GMM-3) [21], which supplies the coefficients of zonal, tesseral, and sectoral harmonics of the Martian gravitational field. These coefficients ($J_{l,m}$ and λ_{lm}) appear in the classical equation of planetary gravitational potentials (per mass unit), written in terms of Legendre polynomials P_{lm},

$$U = \frac{\mu_M}{r} - \frac{\mu_M}{r}\sum_{l=2}^{\infty}\left(\frac{R_M}{r}\right)^l J_l P_{l0}(\sin\varphi) + \frac{\mu_M}{r}\sum_{l=2}^{\infty}\sum_{m=1}^{l}\left(\frac{R_M}{r}\right)^l J_{l,m} P_{lm}(\sin\varphi)\cdot\cos\left[m\left(\lambda_g - \lambda_{lm}\right)\right] \tag{8}$$

where R_M is the mean equatorial radius, whereas λ_g is the spacecraft geographical longitude (taken from the Martian reference meridian). If θ_R denotes the absolute longitude of the reference meridian (taken counterclockwise from $\hat{c}_1$), then the spacecraft geographical longitude is $\lambda_g = \xi - \theta_R$. Both the latitude φ and the absolute longitude ξ can be expressed as functions of the orbit elements by comparing Eqs. (1) and (2). In turn, the latter variables can be written in terms of equinoctial elements using Eq. (3).

In the $(\hat{r}, \hat{E}, \hat{N})$-frame, the gravitational acceleration is given by

$$\underset{\rightarrow}{\mathbf{g}} = \nabla U \quad \text{where} \nabla = \hat{r}\frac{\partial}{\partial r} + \frac{\hat{E}}{r\cos\varphi}\frac{\partial}{\partial\lambda_g} + \frac{\hat{N}}{r}\frac{\partial}{\partial\varphi} \tag{9}$$

The previous expression, together with Eq. (8), leads to obtaining the three components (g_r, g_E, g_N) in the local horizontal $(\hat{r}, \hat{E}, \hat{N})$-frame. Because g_r includes the main gravitational term, the related disturbing acceleration components are $a_r^{(H)} = g_r + \mu/r^2$, $a_E^{(H)} = g_E$, and $a_N^{(H)} = g_N$. Using Eqs. (1) and (2), the components $(a_r^{(H)}, a_\theta^{(H)}, a_h^{(H)})$ of $\underset{\rightarrow}{\mathbf{a}}^{(H)}$ along $(\hat{r}, \hat{\theta}, \hat{h})$ can be obtained in a straightforward way. In this study, all the harmonics associated with $|J_{l,m}| > 10^{-6}$ are considered, i.e. J_2, J_3, J_4, $J_{2,2}$, and $J_{3,1}$.

3.2. Third body perturbation

The gravitational influence of Sun and Jupiter can be modeled as a third body perturbation that affects the space vehicle while it orbits Mars. In general, the perturbing acceleration due to a third body can be expressed as

$$\underset{\rightarrow}{\mathbf{a}}^{(3B)} = -\frac{\mu_3}{s_3^3(1+q_3)^{3/2}}\left[\underset{\rightarrow}{\mathbf{r}} + \underset{\rightarrow}{\mathbf{s}}_3 q_3 \frac{3+3q_3+q_3^2}{1+(1+q_3)^{3/2}}\right] \tag{10}$$

with $q_3 := \left(r^2 - 2\,\underset{\rightarrow}{\mathbf{r}}\cdot\underset{\rightarrow}{\mathbf{s}}_3\right)\Big/ s_3^2$ whereas μ_3 denotes the gravitational parameter of the third body, $\underset{\rightarrow}{\mathbf{s}}_3$ represents its position vector relative to the main body (i.e., Mars), and $s_3 = \left|\underset{\rightarrow}{\mathbf{s}}_3\right|$. The previous expression makes use of the Battin-Giorgi [22,23] approach to the Encke's method for orbit perturbations.

In the MCI-frame, the instantaneous positions of both the Sun and Jupiter can be derived through interpolation of the ephemerides, using the approach described in Ref. 24. Then, $\underset{\rightarrow}{\mathbf{s}}_3$ can be projected onto the LVLH-frame using Eq. (2), to yield the three components of the perturbing acceleration $\underset{\rightarrow}{\mathbf{a}}^{(3B)}$, i.e. $(a_r^{(3B)}, a_\theta^{(3B)}, a_h^{(3B)})$, for each celestial body.

3.3. Solar radiation pressure

Solar radiation pressure is associated with a further perturbing acceleration and derives from the interaction of photons with the spacecraft when it is illuminated. For the sake of simplicity, the cannonball model is adopted [24], and the perturbing acceleration due to solar radiation is

$$\underset{\rightarrow}{\mathbf{a}}^{(SR)} = -\upsilon P_{SR}\frac{c_R S_R}{m}\hat{r}_S \tag{11}$$

where P_{SR} is the solar radiation pressure at Mars, c_R is the radiative coefficient, related to the nature of the radiation interaction with the space vehicle, S_R is the spacecraft cross section that is illuminated, $\hat{r}_S$ is the unit vector aligned with the Sun position vector $\underset{\rightarrow}{\mathbf{a}}^{(3B)}$ (taken from the Mars center), and υ is the shadow function. In this study, c_R is set to 2 (perfect reflection). In the MCI-frame, the instantaneous position of the Sun, $\underset{\rightarrow}{\mathbf{r}}_S$, is interpolated using again the approach described in Ref. 24. Then, $\underset{\rightarrow}{\mathbf{r}}_S$ can be projected onto the LVLH-frame using Eq. (1), to yield the three components of the perturbing accelerations, i.e. $(a_r^{(SR)}, a_\theta^{(SR)}, a_h^{(SR)})$.

The shadow function υ equals either 0 (when the space vehicle is eclipsed) or 1 (when it is illuminated). Letting $\vartheta_1 := \arccos(R_M/r)$, $\vartheta_2 := \arccos(R_M/r_S)$ (with $r_S = \left|\underset{\rightarrow}{\mathbf{r}}_S\right|$), and $\varphi := \arccos(\hat{r}\cdot\hat{r}_S)$, the space vehicle is eclipsed if $\varphi > \vartheta_1 + \vartheta_2$ [24]. Because $R_M/r_S \approx 0$, the previous relation becomes

$$\cos\varphi < -\sin\vartheta_1 = -\sqrt{1-\left(\frac{R_E}{r}\right)^2} \tag{12}$$

The term $\cos\varphi$ can be computed easily, after writing $\hat{r}$ and $\hat{r}_S$ in the MCI-frame. Therefore, if inequality (12) is satisfied, then $\upsilon = 0$, otherwise $\upsilon = 1$.

3.4. Aerodynamic drag

If the spacecraft orbits Mars at relatively low altitudes (lower than 300 km), also the aerodynamic drag is to be considered as a perturbing action. Let S_D and c_D denote the aerodynamic cross section and drag coefficient of the space vehicle. The drag acceleration $\underset{\rightarrow}{\mathbf{a}}^{(D)}$ is given by

$$\underset{\rightarrow}{\mathbf{a}}^{(D)} = -\frac{1}{2}c_D\frac{S_D}{m}\rho v_R\,\underset{\rightarrow}{\mathbf{v}}_R \tag{13}$$

where ρ is the local atmospheric density, $\underset{\rightarrow}{\mathbf{v}}_R$ is the spacecraft velocity relative to the atmosphere, $v_R = \left|\underset{\rightarrow}{\mathbf{v}}_R\right|$, whereas $\beta := m/(c_D S_D)$ is the spacecraft ballistic coefficient. In this research ρ is interpolated by means of a piecewise exponential function, based on tabular data [25]. Further details are provided in Section III.V. As atmospheric arcs are unpowered and are traveled at hypersonic velocities in rarefied flow regime, c_D is nearly constant, as well as β. Under the assumption that the atmosphere rotates together with Mars, the relative velocity is

$$\underset{\rightarrow}{\mathbf{v}}_R = \underset{\rightarrow}{\mathbf{v}} - \omega_M r\cos\varphi\,\hat{E} \tag{14}$$

where $\underset{\rightarrow}{\mathbf{v}}$ denotes the spacecraft inertial velocity, given by $\underset{\rightarrow}{\mathbf{v}} = \sqrt{\mu_M/p}[\hat{r}e\sin f + \hat{\theta}(1+e\cos f)]$, whereas ω_M is the Martian rotation rate. Moreover, $\hat{E}$ can be written as $\hat{E} = \hat{\theta}\cos\zeta - \hat{h}\sin\zeta$, while both φ and ζ can be expressed as functions of the orbit elements by means of Eqs. (1) and (2). These can be written again in terms of equinoctial elements using Eq. (3). As a result, $\underset{\rightarrow}{\mathbf{v}}_R$ can be finally projected in the LVLH-frame, as well as the drag acceleration $\underset{\rightarrow}{\mathbf{a}}^{(D)}$. The respective components are denoted with $(a_r^{(D)}, a_\theta^{(D)}, a_h^{(D)})$.

3.5. Atmospheric modeling

The Martian atmosphere is very rarefied if compared to that of the Earth. For the purpose of investigating aerocapture, appropriate modeling of the atmospheric density is mandatory.

This study uses the Mars Climate Database [25,26] (MCD), which collects a large set of data on the Martian atmospheric density, which depends on (a) altitude h, (b) geographical longitude λ_g, (c) latitude φ, and (d) environmental scenario. The latter includes all the possible conditions related to Martian weather and seasons, affected by the solar activity and depending on the true anomaly of Mars along its orbit. As a result, the dust concentration is subject to considerable variations, and this greatly affects the atmospheric density. On the basis of previous studies and simulations, the *climatology* model was identified as the standard model, based on former observations on dust distribution. Instead, the *cold-scenario* model assumes a very clean atmosphere, with low values of dust opacity and minimum solar activity. On the contrary, the *warm-scenario* model considers high values of dust opacity and maximum solar activity. Finally, the *dust-storm-scenario* model assumes the occurrence of storms over the entire planet and corresponds to the maximum values of density. Moreover, three different options exist for the climatology and the dust-storm-scenario models, associated with (i) minimum, (ii) average, and (iii) maximum solar activity.

Once the most appropriate model is chosen, the density profile is available for the entire planet, at discrete locations $(\lambda_{g,j}, \varphi_k)$ and altitudes $h_{ref,i}$ (in the range [25,125] km). A systematic study was carried out, to evaluate the percentage of variation of the atmospheric density between (a) adjacent (discrete) altitudes and (b) adjacent locations, using 9 comparison points for each location and altitude $(h_{ref,i}, \lambda_{g,j}, \varphi_k)$, i.e.

$$\begin{matrix}\left(h_{ref,i+1}, \lambda_{g,j}, \varphi_k\right), \left(h_{ref,i}, \lambda_{g,j}, \varphi_{k\pm1}\right), \\ \left(h_{ref,i}, \lambda_{g,j\pm1}, \varphi_k\right), \left(h_{ref,i}, \lambda_{g,j\pm1}, \varphi_{k\pm1}\right)\end{matrix} \tag{15}$$

over the entire planet, the percentages of mean and maximum density variations between two adjacent altitudes equal

$$\Delta_{mean}^{(alt)} = 46.8\ \% \quad \text{and } \Delta_{max}^{(alt)} = 56.2\ \% \tag{16}$$

whereas the same quantities referred to adjacent locations (at the same altitude) are

$$\Delta_{mean}^{(loc)} = 14.0\ \% \quad \text{and } \Delta_{max}^{(loc)} = 58.3\ \% \tag{17}$$

It is apparent that considerable variations of the density can be associated with nearby locations at the same altitude. However, if the previous analysis is restricted to the latitudinal range $[-15,15]$ deg, the preceding parameters become

$$\Delta_{mean}^{(loc)} = 0.9\ \% \quad \text{and } \Delta_{max}^{(loc)} = 16.4\ \% \tag{18}$$

Moreover, on average the atmospheric density is greater near the equator. This circumstance, together with the results (18), justifies the choice of restricting the latitudinal range to $[-15,15]$ deg where aerocapture takes place. In this way, the atmospheric density can be assumed to depend only on altitude, other than the specific environmental scenario. This assumption is adopted hence forward. In this research, 4 distinct models, related to different scenarios, are finally identified: (a) climatology, (b) cold, (c) warm, and (d) dust storm. For each model, the minimum and maximum value of density are detected, at all discrete altitudes (in the latitudinal range $[-15,15]$ deg). As a result, for each scenario, two extreme profiles are defined, corresponding to minimum and maximum density. Furthermore, two further density profiles are introduced: (e) the maximum density profile, and (f) the minimum density profile, which respectively contain – for each altitude – the maximum and minimum value of density among all the models. Fig. 1 illustrates 12 density profiles: 4 minimum profiles, 4 mean profiles, and 4 maximum profiles (for models (a)-(d)). The two density profiles (e) and (f) are marked with * and overlap with two of the previous 12 profiles.

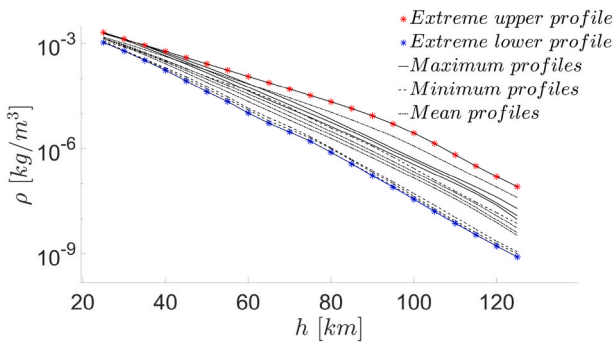

Fig. 1. Atmospheric density profiles using different models.

Because the atmospheric density ρ is available only at discrete altitudes, exponential interpolation is used to provide its values at a generic altitude, i.e.

$$\rho(h) = \rho\left(h_{ref,i}\right)\exp\left[-\frac{h - h_{ref,i}}{H_i}\right] \quad \left(h_{ref,i} \le h \le h_{ref,i+1}\right) \tag{19}$$

where h represents the altitude (with the respective reference values denoted with subscript *ref*), H_i is the scale height, and i identifies a specific altitude interval. In the numerical simulations, stochastic density profiles are generated, by first identifying the interval $[H_i^{(min)}, H_i^{(max)}]$ in which H_i is stochastically described by a uniform distribution. To do this, for each altitude $h_{ref,i}$ the following steps are completed:

(i) for each location, identified by $(\lambda_{g,j}, \varphi_k)$, 9 comparison points are considered (cf. Eq. (15));
(ii) the extremal (minimum and maximum) pair of density values are identified – using all models – for point $(h_{ref,i+1}, \lambda_{g,j}, \varphi_k)$ and all the 9 comparison points, and this leads to identifying the extremal values of H_i for location $(\lambda_{g,j}, \varphi_k)$, denoted with $H_{i,j,k}^{(min)}$ and $H_{i,j,k}^{(max)}$;
(iii) the absolute minimum and maximum values $H_i^{(min)}$ and $H_i^{(max)}$ are identified, by comparing all the values $H_{i,j,k}^{(min)}$ and $H_{i,j,k}^{(max)}$ in the latitudinal range [-15,15] deg.

Then, once the interval $[H_i^{(min)}, H_i^{(max)}]$ is defined at all reference altitudes, the atmospheric density is interpolated through the following two steps:

(i) the atmospheric density $\rho_{ref,1}$ at the minimum altitude (25 km), is selected randomly, assuming uniform distribution in the interval $[\rho_{min,1}, \rho_{max,1}]$;
(ii) in interval i the height scale H_i is selected randomly, assuming uniform distribution in the interval $[H_i^{(min)}, H_i^{(max)}]$.
(iii) at a generic altitude h, $\rho(h)$ is obtained with the use of Eq. (19), with

$$\rho_{ref,i+1} = \rho_{ref,i}\ \exp\left[-\frac{h_{ref,i+1} - h_{ref,i}}{H_i}\right] \tag{20}$$

4. Aerocapture dynamics and maneuvering

Aerocapture begins when the spacecraft enters the Martian atmosphere. Because tabular data on atmospheric density are available for altitudes lower than 125 km, the drag action is assumed to start at this altitude. The reference epoch, corresponding to the time when the spacecraft enters the Martian sphere of influence, is set to January 1, 2025 at 0:00 UT.

The spacecraft is assumed to maintain the same aerodynamic cross section S_D along the atmospheric arc. Moreover, because the space ve-

hicles flies at hypersonic velocities (in a rarefied atmosphere), the drag coefficient c_D is assumed to be constant and equal to 2.2. As a result, the ballistic coefficient $\beta := m/(c_D S_D)$ is constant in each numerical simulation. However, different values of β were considered, to model vehicles with different characteristics. More precisely, β is constrained to the interval $[14.3, 1000]$ Kg/m^2. The upper bound corresponds to a vehicle not designed for aerocapture, such as the Trace Gas Orbiter, whereas the lower bound is defined in relation to the current technological capabilities [27]. The reference surface for the solar radiation pressure is assumed to equal S_D.

The dynamical conditions that precede aerocapture play a crucial role. First, the hyperbolic excess velocity at Mars arrival is constrained to [2,4] km/s [27] (with the special value 3.111 km/s corresponding to Exomars [28]). Second, the periapse altitude of the incoming hyperbola greatly affects aerocapture, and its accurate selection makes it feasible. Due to the choice of the latitudinal region useful for aerocapture, the orbit inclination is constrained to [0,15] deg, whereas the periapse is assumed to lie in the equatorial plane (where density is maximal).

4.1. Aerocapture with no correction maneuver

Aerocapture dynamics are first investigated, under the assumption that the spacecraft performs no correction maneuver. The aerocapture corridor is defined as the interval of periapse altitudes that allows safe aerocapture, i.e. an elliptic orbit (after the atmospheric pass) with apoapse altitude greater than 125 km and not exceeding $0.95 r_{SOI}$, where r_{SOI} denotes the radius of the Martian sphere of influence.

As a preliminary step, the ballistic coefficient β and the hyperbolic excess velocity v_∞ are considered as specified. For each environmental scenario, the maximum- and minimum-density profiles are assumed, and the aerocapture corridors are identified. Several cases are considered, associated with different values of β and v_∞. Fig. 2 – 4 portray the results if $\beta = 14.3, 100, 500$ Kg/m^2 and $v_\infty = 3.111$ km/s. It is apparent that for any scenario no overlapping occurs between the two corridors associated with minimum- and maximum-density profiles (using the same atmospheric model). This result is also apparent from inspection of all the remaining cases considered in this work (and omitted for the sake of brevity), associated with different values of β and v_∞.

The corridor exhibits strong dependency on the hyperbolic excess velocity. This is apparent by inspecting Fig. 5, which depicts the corridor in terms of v_∞, assuming $\beta = 100$ Kg/m^2 and using the minimum-density climatology model. The corridor reduces in width as v_∞ increases. Moreover, both the upper and the lower bounds that define the corridor decrease as v_∞ increases. This behavior is encountered in all cases, i.e. using different atmospheric models and values of β. Due to this, lower values of v_∞ are advantageous to enlarge the aerocapture corridor.

It is rather obvious that the corridor is also affected by β, which is related to the geometrical and mass specifications of the spacecraft. Fig. 6portrays the corridor in terms of β, assuming $v_\infty = 3.111$ km/s and two extremal profiles, corresponding to (a) mimimum-density cold

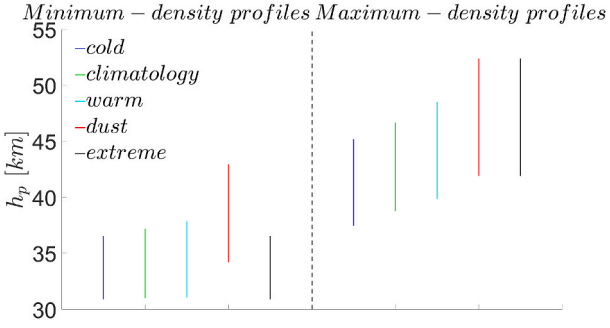

Fig. 2. Aerocapture corridors using different atmospheric models ($\beta = 100$ kg/m^2 and $v_\infty = 3.111$ km/s).

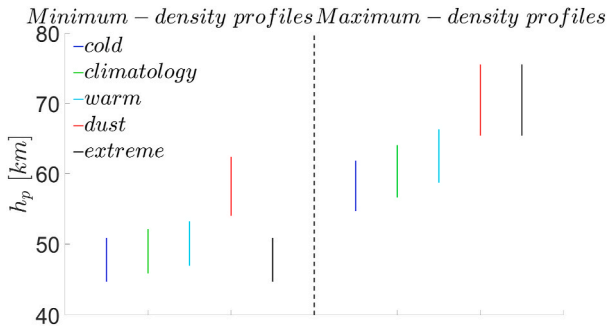

Fig. 3. Aerocapture corridors using different atmospheric models ($\beta = 500$ Kg/m^2 and $v_\infty = 3.111$ km/s).

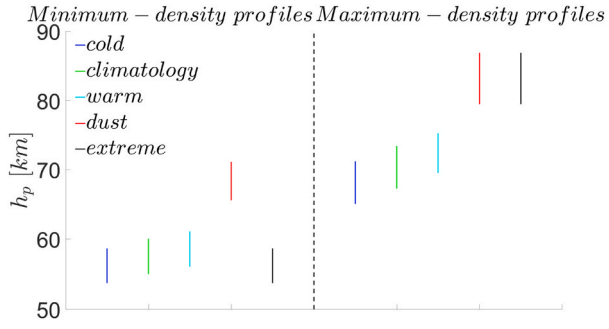

Fig. 4. Aerocapture corridors using different atmospheric models ($\beta = 14.3$ Kg/m^2 and $v_\infty = 3.111$ km/s).

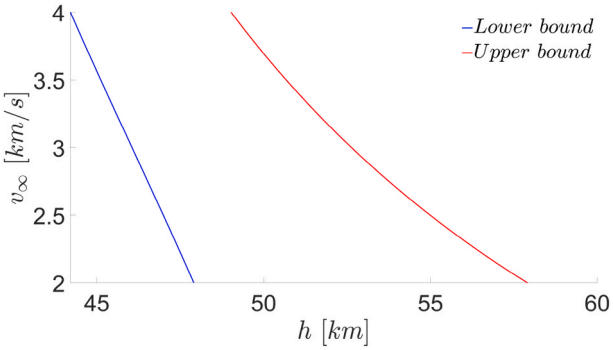

Fig. 5. Aerocapture corridor as a function of v_∞ (assuming $\beta = 100$ Kg/m^2 and minimum-density climatology model).

scenario and (b) maximum-density dust-storm scenario. It is apparent that the aerocapture corridor moves toward higher altitudes as β increases. Moreover, denser atmosphere (case (b)) shifts the aerocapture corridor toward higher altitudes.

A Monte Carlo analysis is performed by assuming uncertain density and initial conditions. Let $\rho_W^{(max)}$ denote the maximum-density profile associated with the warm-scenario model. Stochastic density profiles are generated by assuming that the density varies in the range $[0.7, 1.3]\rho_W^{(max)}$, using the methodology described in Section III.V. Uncertainties on the initial conditions are defined in terms of initial flight-path angle γ (at 125 km of altitude), v_∞, inclination i, RAAN Ω, and argument of periapse ω. Their nominal values are

$$v_\infty = 3.111 \text{ km/s} \quad i = 0 \quad \Omega = 0 \quad \omega = 0 \tag{21}$$

whereas the nominal value of γ is such that the periapse altitude equals the central value of the aerocapture corridor (assuming nominal flight

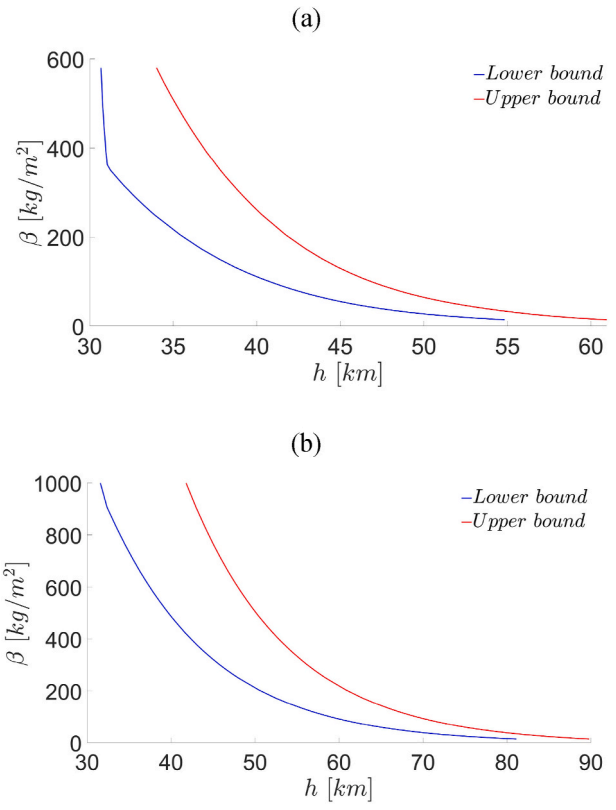

Fig. 6. Aerocapture corridor as a function of β (assuming $v_\infty = 3.111$ km/s and either (a) minimum-density cold model or (b) maximum-density dust-storm model).

conditions). Perturbed variables are randomly generated, with normal distribution, mean value equal to the respective nominal value, and the following standard deviations:

$$\sigma_\gamma = 0.25 \text{ deg} \quad \sigma_{v_\infty} = 0.1 \text{ km/s}$$
$$\sigma_i = \sigma_\Omega = \sigma_\omega = 3 \text{ deg} \tag{22}$$

All of these stochastic quantities are constrained to $[-2\sigma_x, 2\sigma_x]$, where σ_x denotes the respective standard deviation. It is worth remarking that the value of σ_γ roughly corresponds to 1/4 of the entire interval for γ that guarantees aerocapture. After the unpowered atmospheric arc, four possible outcomes are identified:

(1) *capture*,
(2) *near-capture*, if the apoapse altitude exceeds $0.95r_{SOI}$ while $e < 1$,
(3) *escape*, if $e \geq 1$,
(4) *destructive entry*, in all remaining cases.

A Monte Carlo campaign composed of 500000 simulations was run, under the previously described assumptions, with the following percentage outcomes:

(1) 66.0 % (2) 1.4 % (3) 25.6 % (4) 7.0 %.

Although unpowered aerocapture is successful in the majority of the cases, it is apparent that significant percentages are associated with escape trajectories and destructive entry. This circumstance points out the need of designing correction maneuvers, to avoid the undesired outcomes (2) through (4). Although the Monte Carlo analysis is performed by assuming specific uncertainties on the stochastic variables, qualitatively similar results can be expected with similar uncertainties and different (yet still uncertain) density profiles. Considerable increase of the success rate (outcome (1)) is associated with reducing the uncertainties on the atmospheric density and on the initial flight-path angle.

4.2. Correction maneuvers

This subsection is focused on three possible maneuvers aimed at correcting outcomes (2) through (4). They are performed through chemical propulsion, and the impulsive thrust approximation is used as a simplifying assumption. Three types of maneuvers are described in detail, i.e. (a) escape avoidance, (b) corridor selection, and (c) periapse raising. Maneuver (a) is used after the atmospheric pass, if outcome (2) or (3) occurs, whereas maneuver (b) is to be performed before the atmospheric arc, and is particularly suitable for avoiding outcome (4). The third maneuver (c) consists of increasing the periapse altitude to 140 km at the first apoapse.

Escape avoidance maneuver. After the atmospheric arc, the spacecraft is assumed to travel a hyperbolic path (condition (3)) or a near-capture elliptic orbit (condition (2)). In both cases, an in-plane impulsive velocity change is applied to reduce the orbit eccentricity and obtain the desired apoapse radius $r_a (= 0.95r_{SOI})$. The maneuver at hand minimizes

$$J = \Delta v_r^2 + \Delta v_\theta^2 \tag{23}$$

while holding

$$a(1+e) - r_a = 0 \tag{24}$$

where $\Delta v_r = v_r - v_{r,i}$ and $\Delta v_\theta = v_\theta - v_{\theta,i}$; v_r and v_θ denote the two velocity components in the LVLH-frame, and subscript i indicates their values prior to the impulse. Using the expressions of the angular momentum and the vis-viva equation for energy, Eq. (24) becomes

$$f(v_r, v_\theta) = v_r^2 + \left(1 - \frac{r_i^2}{r_a^2}\right) v_\theta^2 + 2\mu\left(\frac{1}{r_a} - \frac{1}{r_i}\right) = 0 \tag{25}$$

The constraint equation is added to the objective function, to yield the extended function

$$\widetilde{J} = \left(v_r - v_{r,i}\right)^2 + \left(v_\theta - v_{\theta,i}\right)^2 + \lambda f(v_r, v_\theta) \tag{26}$$

where λ is the Lagrange multiplier associated with the constraint equation (25). This constrained optimization problem yields the following conditions for a stationary solution:

$$v_r = \frac{A}{A+\lambda} v_{r,i} \tag{27}$$

$$v_\theta = \frac{B}{B+\lambda} v_{\theta,i} \tag{28}$$

$$\frac{v_r^2}{A} + \frac{v_\theta^2}{B} - 1 = 0 \tag{29}$$

where

$$A = \frac{1}{2\mu}\left(\frac{1}{r_i} - \frac{1}{r_a}\right)^{-1} \quad B = A\left(1 - \frac{r_i^2}{r_a^2}\right)^{-1} \tag{30}$$

Insertion of Eqs. (27) and (28)into Eq. (29) yields a 4-th degree equation for λ, which finally leads to identifying the minimizing values of (v_r, v_θ), by means of Eqs.(27) and (28). Because the constraint equation (25), also rewritten in the form (29), is associated with an ellipse in the (v_r, v_θ)-plane (cf. Fig. 7), the minimization problem corresponds to finding the minimum-distance segment that connects $(v_{r,i}, v_{\theta,i})$ to the constraint ellipse.

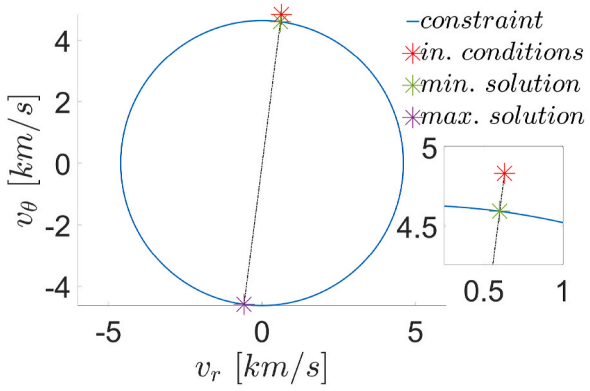

Fig. 7. Constraint ellipse and minimum-Δv segment in the (v_r, v_θ)-plane (with zoom in the inset).

Corridor selection maneuver. Before the atmospheric arc, the spacecraft travels a hyperbolic path. At a specified point, corresponding to $(r_i, v_{r,i}, v_{\theta,i})$ an impulsive velocity change is applied, to obtain the desired peripase radius r_p. The maneuver at hand minimizes

$$J = \Delta v_r^2 + \Delta v_\theta^2 \tag{31}$$

while holding

$$a(1-e) - r_p = 0 \tag{32}$$

Using again the expressions of the angular momentum and the vis-viva equation for energy, Eq. (32) becomes

$$g(v_r, v_\theta) = v_r^2 + \left(1 - \frac{r_i^2}{r_p^2}\right) v_\theta^2 + 2\mu\left(\frac{1}{r_p} - \frac{1}{r_i}\right) = 0 \tag{33}$$

$$\widetilde{J} = \left(v_r - v_{r,i}\right)^2 + \left(v_\theta - v_{\theta,i}\right)^2 + \lambda g(v_r, v_\theta) \tag{34}$$

where λ is the Lagrange multiplier associated with the constraint equation (33). This constrained optimization problem yields the following conditions for a stationary solution:

$$v_r = \frac{C}{C+\lambda} v_{r,i} \tag{35}$$

$$v_\theta = \frac{D}{D-\lambda} v_{\theta,i} \tag{36}$$

$$\frac{v_r^2}{C} - \frac{v_\theta^2}{D} + 1 = 0 \tag{37}$$

where

$$C = \frac{1}{2\mu}\left(\frac{1}{r_p} - \frac{1}{r_i}\right)^{-1} \quad D = -C\left(1 - \frac{r_i^2}{r_p^2}\right)^{-1} \tag{38}$$

Insertion of Eqs. (35) and (36) into Eq. (37) yields a 4-th degree polynomial equation for λ, which finally leads to identifying the minimizing values of (v_r, v_θ) by means of Eqs. (35) and (36). Because the constraint equation, also rewritten in the form (37), is associated with a hyperbola in the (v_r, v_θ)-plane, the minimization problem corresponds to finding the minimum-distance segment that connects $(v_{r,i}, v_{\theta,i})$ to the constraint hyperbola (cf. Fig. 8). However, the desired periapse is defined in relation to the initial specific energy along the approaching hyperbolic trajectory. In general, an impulsive velocity change alters energy, unless

$$v_r^2 + v_\theta^2 = v_{r,i}^2 + v_{\theta,i}^2 = E^2 \tag{39}$$

The latter relation is associated with a circle of radius E in the (v_r, v_θ)-plane. Fig. 8 portrays an illustrative sketch of the geometrical

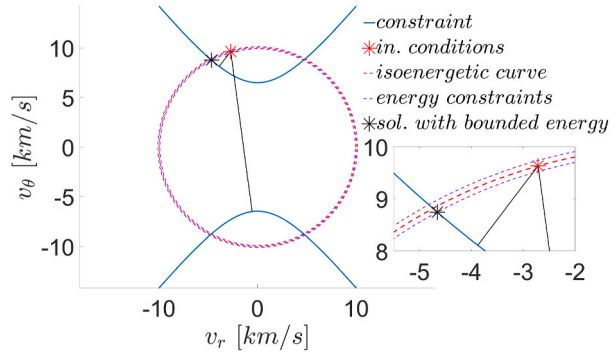

Fig. 8. Constraint hyperbola and minimum-Δv solutions in the (v_r, v_θ)-plane (with zoom in the inset).

interpretation of the minimization problem. The blue lines are two arcs of hyperbola, associated with constraint (37), whereas the red dotted circle corresponds to Eq. (39). Two stationary solutions are shown (black lines). The upper segment is the minimizing solution (also visible in the inset). If the constraint (39) is enforced (with a certain tolerance, cf. purple dotted lines in the inset), then the solution marked with black * in the inset is to be selected.

Efficiency of this impulsive maneuver can be expected to reduce as the spacecraft approaches the Martian atmosphere. In fact, Pontani [29] proved that the velocity variation needed to change the periapse of an incoming hyperbola tends to zero as the distance from the main attracting body tends to infinity. However, in practical scenarios velocity changes occur at finite distances. Fig. 9 illustrates the velocity variation needed to change the periapse altitude from its initial value (30 km) to any other altitude in the range [25,125] km, assuming different hyperbolic excess velocities and maneuver at the Martian sphere of influence (without taking into account the constraint (39)). Fig. 10 portrays the same plots if the maneuver takes place at 125 km of altitude. It is apparent that in the latter case the velocity change increases dramatically, and this testifies to the convenience of performing early corridor selection maneuvers.

Periapse raising maneuver. After the atmospheric arc, the spacecraft may be traveling a near-circular orbit. In this case, low-thrust propulsion does not suffice to raise the periapse (after the first pass) before the subsequent periapse pass, and the spacecraft is subject to repeating atmospheric passes, which finally lead to destructive entry. To avoid this, an impulsive velocity change is applied (tangentially) at apoapse, to raise the periapse altitude to 140 km. More specifically, the periapse raising maneuver is performed when eccentricity is less than 0.45 (threshold value found through numerical analysis).

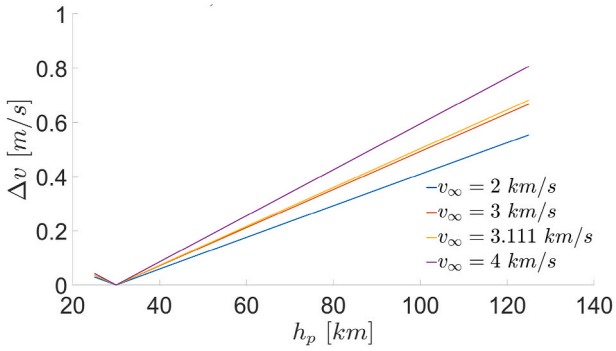

Fig. 9. Velocity change (at the sphere of influence) needed to modify the periapse altitude.

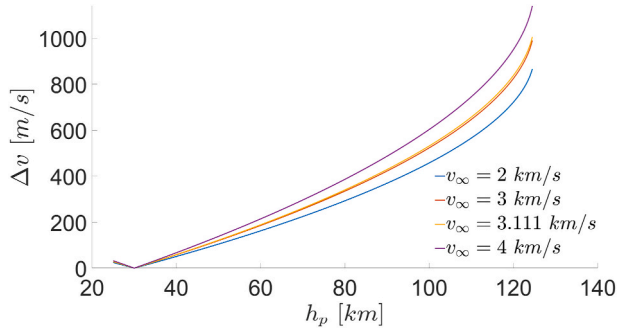

Fig. 10. Velocity change (at the atmospheric boundary, altitude of 125 km) needed to modify the periapse altitude.

5. Nonlinear orbit control

Nonlinear orbit control represents a valid strategy to drive the spacecraft toward the final operational orbit, starting from dispersed initial conditions, after the atmospheric arc.

In a preceding section, the spacecraft motion was shown to be governed by Eqs. (4), (5) and (7). In particular, Eq. (4) can be rewritten as

$$\dot{z} = \mathbf{G}(z, x_6)\left(\frac{\boldsymbol{u}_T}{x_7} + \boldsymbol{a}_P\right) \tag{40}$$

where the perturbing acceleration $\boldsymbol{a}_P$ includes the perturbing contributions related to the space environment. It is worth noticing that Eq. (40) assumes a control-affine form in the absence of perturbing accelerations ($\boldsymbol{a}_P = \mathbf{0}$). For systems governed by Eq. (40) with $\boldsymbol{a}_P = \mathbf{0}$, the Jurdjevic-Quinn theorem provides a feedback control law that can drive the dynamical system to an arbitrary target state, making the controlled system Lyapunov-stable.

The desired operational conditions related to the target orbit are assumed to depend only on z (cf. Eq. (3)) and can be formally defined by

$$\boldsymbol{\psi}(z) = \mathbf{0} \tag{41}$$

The previous vector equation is problem-dependent and corresponds to q (≤ 5) relations that involve equinoctial elements x_1 through x_5. If $q < 5$, Eq. (41) identifies a target set that is assumed to be a connected and differentiable manifold. In this subsection, the operational orbit is specified in terms of its semimajor axis, eccentricity, and inclination, or, equivalently, periapse and apoapse radii, denoted respectively with $r_{P,d}$ and $r_{A,d}$, and inclination i_d. Due to the definitions of Eq. (3), this means that the desired operational conditions correspond to

$$x_1 - r_{P,d}\left(1 + \sqrt{x_2^2 + x_3^2}\right) = 0 \tag{42}$$

$$x_1 - r_{A,d}\left(1 - \sqrt{x_2^2 + x_3^2}\right) = 0 \tag{43}$$

$$x_4^2 + x_5^2 - \tan^2\frac{i_d}{2} = 0 \tag{44}$$

The left-hand sides of Eqs. (42)-(44) are denoted with (ψ_1, ψ_2, ψ_3) and form the vector $\boldsymbol{\psi}$. The spacecraft motion is governed by Eqs. (5), (7) and (40).

A feedback control law is sought that is capable of driving the dynamical system at hand (associated with Eqs. (5), (7) and (40)) toward the target conditions identified by Eq. (41). To do this, the following candidate Lyapunov function is introduced:

$$V = \frac{1}{2}\boldsymbol{\psi}^T \mathbf{K} \boldsymbol{\psi} \tag{45}$$

where $\mathbf{K}$ denotes a diagonal matrix with constant, positive elements, which play the role of arbitrary weights. These are selected a priori in relation to the application of interest. It is clear that $V > 0$ unless $\boldsymbol{\psi} = \mathbf{0}$. Yet, further conditions are required in order that V be an actual Lyapunov function. Three propositions, whose proofs are reported in Ref. 30, provide the theoretical background to identify a saturated feedback law.

Proposition 1. *Let $\boldsymbol{b} := \mathbf{G}^T(\partial\boldsymbol{\psi}/\partial z)^T\mathbf{K}\boldsymbol{\psi}$. If and $\boldsymbol{\psi}$ and $(\partial\boldsymbol{\psi}/\partial z)$ are continuous, $|\boldsymbol{b}| > 0$ unless $\boldsymbol{\psi} = \mathbf{0}$, and $u_T^{(max)} \geq x_7|\boldsymbol{b} + \boldsymbol{a}_P|$, then the feedback control law*

$$\boldsymbol{u}_T = -x_7(\boldsymbol{b} + \boldsymbol{a}_P) \tag{46}$$

leads a dynamical system governed by Eqs. (5), (7) and (40) to converge asymptotically to the target set associated with Eq. (41).

The previous proposition includes the assumption $u_T^{(max)} \geq x_7|\boldsymbol{b} + \boldsymbol{a}_P|$. If this condition is violated, the feedback control law (46) is infeasible, because $|\boldsymbol{u}_T| = x_7|\boldsymbol{b} + \boldsymbol{a}_P|$ would exceed the maximal value $u_T^{(max)}$. In this case, in place of (46), an alternative feedback law can be used.

Proposition 2. *Let $\boldsymbol{b} := \mathbf{G}^T(\partial\boldsymbol{\psi}/\partial z)^T\mathbf{K}\boldsymbol{\psi}$. If and $\boldsymbol{\psi}$ and $(\partial\boldsymbol{\psi}/\partial z)$ are continuous, $|\boldsymbol{b}| > 0$ unless $\boldsymbol{\psi} = \mathbf{0}$, $u_T^{(max)} < x_7|\boldsymbol{b} + \boldsymbol{a}_P|$, and $\boldsymbol{b}^T\boldsymbol{a}_P \leq 0$, then the feedback control law*

$$\boldsymbol{u}_T = -u_T^{(max)}\frac{\boldsymbol{b} + \boldsymbol{a}_P}{|\boldsymbol{b} + \boldsymbol{a}_P|} \tag{47}$$

leads a dynamical system governed by Eqs. (5), (7) and (40) to converge asymptotically to the target set associated with Eq. (41).

It is worth remarking that the previous proposition requires the sufficient condition $\boldsymbol{b}^T\boldsymbol{a}_P \leq 0$ to ensure $\dot{V} < 0$. An additional sufficient condition that ensures $\dot{V} < 0$ even if $\boldsymbol{b}^T\boldsymbol{a}_P > 0$, regardless of the specific time evolution, is provided by the following

Proposition 3. *Let $\boldsymbol{b} := \mathbf{G}^T(\partial\boldsymbol{\psi}/\partial z)^T\mathbf{K}\boldsymbol{\psi}$. If and $\boldsymbol{\psi}$ and $(\partial\boldsymbol{\psi}/\partial z)$ are continuous, $|\boldsymbol{b}| > 0$ unless $\boldsymbol{\psi} = \mathbf{0}$, and $x_7|\boldsymbol{a}_P| < u_T^{(max)} < x_7|\boldsymbol{b} + \boldsymbol{a}_P|$, then the feedback control law (47) leads a dynamical system governed by Eqs. (5), (7) and (40) to converge asymptotically to the target set associated with Eq. (41).*

The two feedback laws (46) and (47) can be written in compact form as

$$\boldsymbol{u}_T = -u_T^{(max)}\frac{x_7(\boldsymbol{b} + \boldsymbol{a}_P)}{\max\left\{u_T^{(max)}, x_7|\boldsymbol{b} + \boldsymbol{a}_P|\right\}} \tag{48}$$

Equation (48) incorporates the saturation condition on $\boldsymbol{u}_T$, i.e. $|\boldsymbol{u}_T| \leq u_T^{(max)}$, and provides a control law that can be actuated using steerable and throttleable propulsive thrust (with time-varying magnitude and direction).

Proposition 3 provides a very useful sufficient condition that has a straightforward meaning: if the thrust acceleration magnitude, $u_T^{(max)}/x_7$, exceeds the perturbation acceleration magnitude, a_P, then $\dot{V} < 0$ unless $\boldsymbol{\psi} = \mathbf{0}$. As a final remark, it is worth stressing that Propositions 1 through 3 state some sufficient conditions for Lyapunov stability. This circumstance implies that the assumptions of Propositions 1 through 3 can be violated (in some time intervals), without necessarily compromising asymptotic convergence to the desired final condition identified by Eq. (41).

As first steps, both $\boldsymbol{\psi}$ and $(\partial\boldsymbol{\psi}/\partial z)$ turn out to be continuous in the entire domain where equinoctial elements are defined (i.e., $i \neq \pi$).

Then, vector $\boldsymbol{b}$, whose components are $\{b_1, b_2, b_3\}$, is derived analytically. The related expressions are

$$b_1 = \sqrt{\frac{x_1}{\mu_M}}\,\frac{x_3\cos x_6 - x_2\sin x_6}{\sqrt{x_2^2 + x_3^2}}\left(k_1\psi_1 r_{P,d} - k_2\psi_2 r_{A,d}\right) \tag{49}$$

$$b_2 = \sqrt{\frac{x_1}{\mu_M}}\left[\left(\frac{\sqrt{x_2^2+x_3^2}}{\eta}+\frac{x_2\cos x_6 + x_3 \sin x_6}{\sqrt{x_2^2+x_3^2}}\frac{1+\eta}{\eta}\right)\cdot\right.$$
$$\left.\cdot\left(k_2\psi_2 r_{A,d} - k_1\psi_1 r_{P,d}\right)+\frac{2x_1}{\eta}\left(k_1\psi_1+k_2\psi_2\right)\right] \tag{50}$$

$$b_3 = \sqrt{\frac{x_1}{\mu_M}}k_3\psi_3\left(1+x_4^2+x_5^2\right)\frac{x_4\cos x_6 + x_5 \sin x_6}{\eta} \tag{51}$$

The two terms with $\sqrt{x_2^2+x_3^2}$ in the denominator can be proven to be constrained to the interval $[-1,1]$. In fact, the following identities hold:

$$\frac{x_3\cos x_6 - x_2 \sin x_6}{\sqrt{x_2^2+x_3^2}} = -\sin f \tag{52}$$

$$\frac{x_2\cos x_6 + x_3 \sin x_6}{\sqrt{x_2^2+x_3^2}} = \cos f \tag{53}$$

The attracting set collects all the dynamical states that fulfill $\dot{V} = 0$. In fact, out of the attracting set $\dot{V} < 0$. The latter condition is met if $\boldsymbol{b} = \mathbf{0}$, i.e. if the three components $\{b_1, b_2, b_3\}$ equal 0, for any choice of the positive coefficients $\{k_1, k_2, k_3\}$. Inspection of Eq. (49) reveals that $b_1 = 0$ (regardless of $\{k_1,\ k_2\}$) if $((\psi_1 = 0)$ and $(\psi_2 = 0))$ or $(x_3\cos x_6 - x_2 \sin x_6 = 0)$. However, the second equality is ruled out, because x_6 is always time-varying (even in the target set). Then, the condition $((\psi_1 = 0)$ and $(\psi_2 = 0))$ also ensures that $b_2 = 0$. Finally, $b_3 = 0$ if $(\psi_3 = 0)$ or $(x_4 = x_5 = 0)$ or $(x_4\cos x_6 + x_5 \sin x_6 = 0)$. The latter equality is again ruled out because x_6 is time-varying. In conclusion, the attracting set turns out to include the following three subsets:

1. $x_1 = 0$ (rectilinear trajectories);
2. $\psi_1 = 0, \psi_2 = 0$, and $x_4 = x_5 = 0$ (equatorial orbits with periapse and apoapse radii equal to $r_{P,d}$ and $r_{A,d}$);
3. $\psi_1 = 0$, $\psi_2 = 0$, and $\psi_3 = 0$ (operational conditions, cf. Eqs. (42)-(44)).

Because the attracting set contains other subsets other than the target set (which coincides with subset 3), the asymptotic convergence toward the desired conditions is only local, based on Lyapunov's stability theorem [31].

However, LaSalle's principle [31] can be applied in order to rule out, if possible, subsets 1 and 2. Because $\boldsymbol{\psi}$ is continuous and $\dot{V} < 0$ (except in the attracting set, denoted with A henceforth), the condition $V(\boldsymbol{z}) \leq V(\boldsymbol{z}_0)$ (where $\boldsymbol{z}_0$ is $\boldsymbol{z}$ evaluated at the initial time) defines a compact set C. The invariant set, which plays a crucial role in LaSalle's principle, is to be sought in $\mathrm{A} \cap \mathrm{C}$, i.e. in the portion of the attracting set contained in C. By definition, the invariant set collects all the dynamical states (in the attracting set of $\boldsymbol{z}$) that remain unaltered when $\boldsymbol{a} \equiv \mathbf{0}$. This means that once the invariant set is reached, $\boldsymbol{b} \equiv \mathbf{0}$ at future times, which implies $\dot{\boldsymbol{b}} \equiv \mathbf{0}$ while $\boldsymbol{a} \equiv \mathbf{0}$. For the application at hand, the time derivatives of the three components of $\boldsymbol{b}$, evaluated at $\boldsymbol{a} \equiv \mathbf{0}$, assume the form

$$\dot{b}_j = \frac{\partial b_j}{\partial x_6}\sqrt{\frac{\mu_E}{x_1^3}}\eta^2 \ (j = 1,2,3) \tag{54}$$

Inspection of $\dot{b}_j$ $(j = 1,2,3)$, whose lengthy expressions are omitted for the sake of brevity, leads to ruling out subset 1 ($x_1 = 0$), associated with rectilinear trajectories Instead, both subsets 2 and 3 form the invariant set for the problem at hand.

Actually, convergence toward subset 2 is only theoretical. In fact, the Lyapunov function can be rewritten in terms of orbit elements as

$$V = \frac{1}{2}k_1\left[p - r_{P,d}(1+e)\right]^2 + \frac{1}{2}k_2\left[p - r_{A,d}(1-e)\right]^2 + \frac{1}{2}k_3\left(\tan^2\frac{i}{2} - \tan^2\frac{i_d}{2}\right)^2 \tag{55}$$

where p, e, and i are the instantaneous semilatus rectum, eccentricity, and inclination. The partial derivative of V with respect to i is

$$\frac{\partial V}{\partial i} = k_3 \tan\frac{i}{2}\left(\tan^2\frac{i}{2}+1\right)\left(\tan^2\frac{i}{2} - \tan^2\frac{i_d}{2}\right) \tag{56}$$

It is apparent that $\partial V/\partial i = 0$ (i.e. V is stationary) at $i = 0$, which is consistent with the fact that subset 2 belongs to the invariant set. However, if $i = i_\epsilon > 0$ (with i_ϵ arbitrarily small), then $\partial V/\partial i < 0$, and the reduction of V leads i to increasing up to the desired value i_d, which is associated with subset 3, i.e. the target set. This means that the target set represents a stable equilibrium, unlike set 2. This circumstance has the very interesting practical consequence that – from the numerical point of view – the dynamical system of interest enjoys global convergence toward the desired operational conditions, provided that the control law (48) is adopted, while holding the assumptions of either Proposition 1, 2, or 3.

6. Orbit injection: numerical simulations

This research considers three final orbits.

(a) areostationary orbit,
(b) quasi-synchronous, circular, direct orbit, and
(c) sunsynchronous circular orbit.

All orbits (a) through (c) are defined in terms of their semilatus rectum, eccentricity, and inclination.

This section is focused on presenting the numerical simulations of the entire orbit injection maneuver, composed of four major phases: (i) selection of the aerocapture corridor, (ii) atmospheric arc, (iii-a) escape avoidance maneuver or (iii-b) periapse raising, and (iv) low-thrust nonlinear orbit control. The impulsive maneuvers (i), (iii-a), and (iii-b) are performed only if necessary. Numerical simulations prove that maneuver (iii-a) is unnecessary with outcome 2 (near-capture).

The low-thrust system (used in phase (iv)) has the following characteristic parameters:

$$c = 30 \text{ km/s}, u_T^{(max)} = 5{\cdot}10^{-5}\mathrm{g}_0 \ (\mathrm{g}_0 = 9.8 \text{ m/s}^2)$$

Instead, because the impulsive thrust approximation is adopted to model the effect of chemical propulsion, only the effective exhaust velocity c_{HT} of the high-thrust (chemical) system (used in phases (i) and (iii)) is needed to evaluate the resulting mass depletion. In this study, $c_{HT} = 3.528$ km/s.

In all cases the atmospheric density profile is generated stochastically in the range $[0.6, 1.4]\rho_C^{(max)}$, where $\rho_C^{(max)}(h)$ represents the maximum-density profile of the climatology model. The nominal flight-path angle is such that the central periapse altitude of the corridor is targeted. Moreover, the following values are assumed for β and v_∞:

$$\beta = [14.3, 33.3, 100, 500, 1000] \text{ Kg/m}^2 \tag{57}$$

$$v_\infty = [2, 3, 3.111, 4] \text{ km/s} \tag{58}$$

For each pair of values of (β, v_∞), 5 Monte Carlo simulations are performed, using a random displacement for the initial flight-path angle, with zero mean and standard deviation $\sigma_\gamma = 0.25$ deg. This process generates 100 simulations. Based on this, for each final orbit, a total number of 300 simulations are performed: (1) 100 associated with natural capture, (2) 100 corresponding to near-capture, and (3) 100

Table 1
Injection into areostationary orbit: performance for trajectories with outcome 1 (capture) after the atmospheric arc.

	Mean value	Standard deviation
t_f	44 days	21 days
MR	0.948	0.032
Δv_{apo}	19 m/s	5 m/s

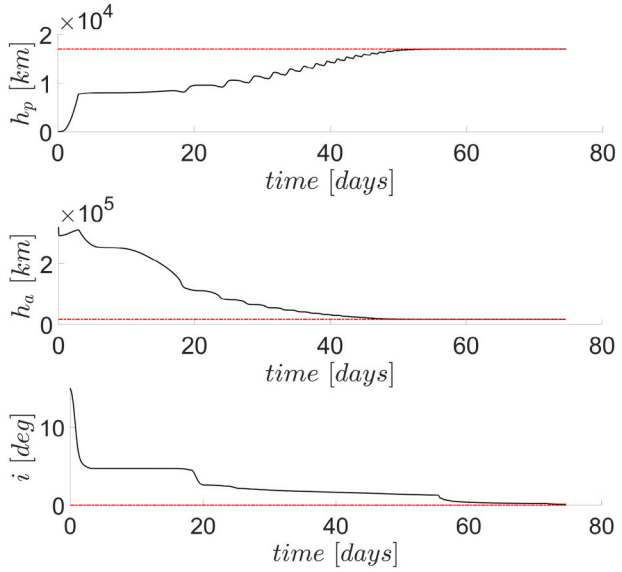

Fig. 11. Injection in areostationary orbit: time histories of periapse and apoapse radii, and inclination (single MC simulation).

associated with escape. Capture, near-capture and escape refer to natural motion, in the absence of propulsion correction maneuvers.

6.1. Final areostationary orbit

The areostationary orbit corresponds to the following elements:

$$p_d = 20428 \text{ km} \quad e_d = 0 \quad i_d = 0 \text{ deg} \tag{59}$$

A Monte Carlo campaign composed of 300 simulations was run, and the related results are collected in Table 1 – 3, where MR is the final mass ratio, Δv_{apo} denotes the velocity change to perform periapse raising, and Δv_{ext} represents the velocity variation to avoid escape (see Fig. 10). Periapse raising was needed in 24 cases out of 100, and the statistics in Table 1 refer to these 24 simulations only. Fig. 11 depicts the time histories of periapse and apoapse altitudes, and inclination, for a single simulation.

The performance of the preceding strategy is compared to a more traditional approach, based on applying a single velocity change at a periapse altitude of 500 km (to get planetary capture), followed by low-thrust. The latter strategy yields the following results:

$$\begin{aligned} v_\infty &= 2 \text{ km/s} : MR = 0.829 \text{ and } t_f = 56.1 \text{ days} \\ v_\infty &= 4 \text{ km/s} : MR = 0.614 \text{ and } t_f = 46.2 \text{ days} \end{aligned} \tag{60}$$

Table 2
Injection into areostationary orbit: performance for trajectories with outcome 2 (near capture) after the atmospheric arc.

	Mean value	Standard deviation
t_f	69 days	4 days
MR	0.930	0.003
Δv_{ext}	0 m/s	0 m/s

Table 3
Injection into areostationary orbit: performance for trajectories with outcome 3 (escape) after the atmospheric arc.

	Mean value	Standard deviation
t_f	59 days	2 days
MR	0.884	0.039
Δv_{ext}	202 m/s	158 m/s

It is apparent that aerocapture followed by low-thrust nonlinear orbit control is more advantageous than the traditional strategy.

6.2. Final quasi-synchronous orbit

The quasi-synchronous orbit represents a valuable option for satellite constellations [32], and corresponds to the following elements:

$$p_d = 32427 \text{ km} \quad e_d = 0 \quad i_d = 60.0 \text{ deg} \tag{61}$$

A Monte Carlo campaign composed of 300 simulations was run, and the related results are collected in Table 4 – 6, whereas Fig. 12 depicts the time histories of periapse and apoapse altitudes, and inclination, for a single simulation. Periapse raising was needed in 40 cases out of 100, and the statistics in Table 4 refer to these 40 simulations only.

The performance of the preceding strategy is compared again to a more traditional approach, based on applying a single velocity change at a periapse altitude of 500 km (to get planetary capture), followed by low-thrust. The latter strategy yields the following results:

$$\begin{aligned} v_\infty &= 2 \text{ km/s} : MR = 0.802 \text{ and } t_f = 74.7 \text{ days} \\ v_\infty &= 4 \text{ km/s} : MR = 0.591 \text{ and } t_f = 60.8 \text{ days} \end{aligned} \tag{62}$$

It is apparent that aerocapture followed by low-thrust nonlinear orbit control is more advantageous, while the traditional strategy approaches

Table 4
Injection into quasi-synchronous orbit: performance for trajectories with outcome 1 (capture) after the atmospheric arc.

	Mean value	Standard deviation
t_f	83days	21 days
MR	0.884	0.034
Δv_{apo}	21 m/s	11 m/s

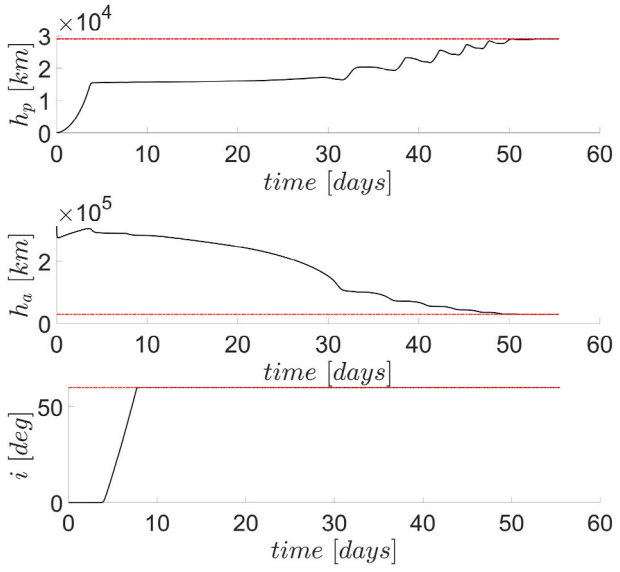

Fig. 12. Injection in quasi-synchronous orbit: time histories of periapse and apoapse radii, and inclination (single MC simulation).

Table 5
Injection into quasi-synchronous orbit: performance for trajectories with outcome 2 (near capture) after the atmospheric arc.

	Mean value	Standard deviation
t_f	123 days	22 days
MR	0.878	0.013
Δv_{ext}	0 m/s	0 m/s

the worst-case result (MR) obtained with aerocapture and low thrust only if $v_\infty = 2$ km/s.

6.3. Final sunsynchronous orbit

A sunsynchronous orbit is considered, associated with the following elements:

$$p_d = 3897 \text{ km} \quad e_d = 0 \quad i_d = 93.2 \text{ deg} \tag{63}$$

A Monte Carlo campaign composed of 300 simulations was run, and the related results are collected in Table 7 – 9, where Fig. 13 depicts the time histories of periapse and apoapse altitudes, and inclination, for a single simulation. Periapse raising was needed in 22 cases out of 100, and the statistics in Table 7 refer to these 22 simulations only.

The performance of the preceding strategy is compared again to a more traditional approach, based on applying a single velocity change at a periapse altitude of 500 km (to get planetary capture), followed by low-thrust. The latter strategy yields the following results:

$$\begin{aligned} &v_\infty = 2 \text{ km/s} : MR = 0.743 \text{ and } t_f = 120.5 \text{ days} \\ &v_\infty = 4 \text{ km/s} : MR = 0.371 \text{ and } t_f = 203.5 \text{ days} \end{aligned} \tag{64}$$

It is apparent that aerocapture followed by low-thrust nonlinear orbit control is more advantageous, while the traditional strategy approaches the worst-case result (MR) obtained with aerocapture and low thrust only if $v_\infty = 2$ km/s.

6.4. Corridor selection maneuver

Correction maneuver (ii), aimed at selecting the aerocapture corridor, is particularly effective for the purpose of recovering trajectories otherwise ending with destructive entry. However, sufficiently accurate information on the density profile is needed to successfully perform this maneuver. Moreover, instead of pursuing the central periapse altitude of the nominal corridor $[h_p^{(min)}, h_p^{(max)}]$, the periapse altitude $0.75\, h_p^{(max)}$ is targeted. This is an interesting option because the possible subsequent maneuver (escape avoidance) is simpler and much more economical than performing an atmospheric recovery maneuver (not described in Section IV.II) in the case of excessive braking.

Table 6
Injection into quasi-synchronous orbit: performance for trajectories with outcome 3 (escape) after the atmospheric arc.

	Mean value	Standard deviation
t_f	79 days	3 days
MR	0.858	0.040
Δv_{ext}	185 m/s	167 m/s

Table 7
Injection into sunsynchronous orbit: performance for trajectories with outcome 1 (capture) after the atmospheric arc.

	Mean value	Standard deviation
t_f	138 days	32 days
MR	0.805	0.047
Δv_{apo}	18 m/s	4 m/s

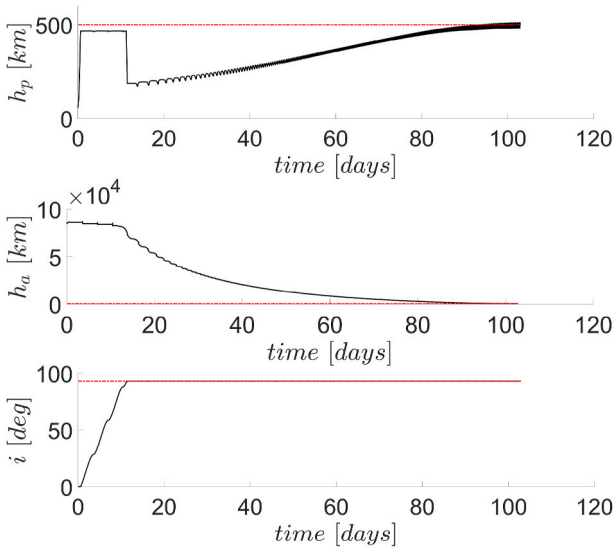

Fig. 13. Injection in sunsynchronous orbit: time histories of periapse and apoapse radii, and inclination (single MC simulation).

Table 8
Injection into sunsynchronous orbit: performance for trajectories with outcome 2 (near capture) after the atmospheric arc.

	Mean value	Standard deviation
t_f	138 days	0,4 days
MR	0.836	0.001
Δv_{ext}	8 m/s	5 m/s

Table 9
Injection into sunsynchronous orbit: performance for trajectories with outcome 3 (escape) after the atmospheric arc.

	Mean value	Standard deviation
t_f	132 days	4 days
MR	0.786	0.037
Δv_{ext}	222 m/s	164 m/s

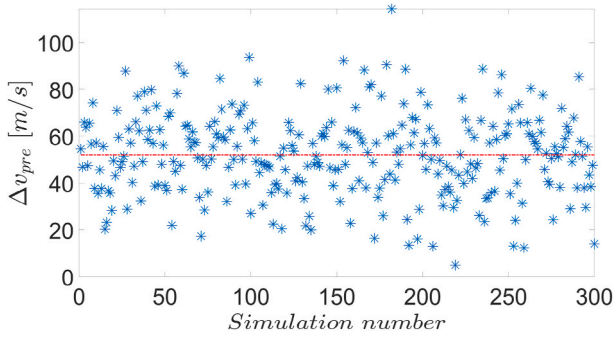

Fig. 14. Velocity changes for corridor selection.

This subsection presents the results of 100 Monte Carlo simulations, starting for initial conditions that would lead to destructive entry. All the initial conditions coincide with those described at the beginning of Section VI, with the only exception that the density profile uncertainty is constrained to $[0.9, 1.1]\rho_C^{(max)}$.

Fig. 14 depicts the magnitude of the velocity changes needed to select the aerocapture corridor, according to the preceding assumptions and methodology. The velocity variation, which is assumed to occur at 125 km of altitude, has average value and standard deviation equal to 52 m/s and 17 m/s, respectively. It is worth remarking that greater uncertainty in the atmospheric density may render the use of a single velocity change ineffective for the purpose of avoiding destructing entry. In this case, repeating velocity variations shall be applied, in the context of an iterative feedback guidance scheme, while the density estimation is refined during descent.

6.5. Technological challenges

Aerocapture, in conjunction with low-thrust propulsion, can be regarded as a viable option to perform Mars orbit injection. However, significant technological challenges may be associated with this strategy. If solar electric propulsion (SEP) is employed, then the solar panels can be either (i) arranged on the sides of the spacecraft or (ii) initially stowed and deployed only after the atmospheric pass. In case (i) they must not be subject to the aerodynamic interaction. In case (ii), they are to be deployed after aerocapture, to guarantee sufficient power to the low-thrust propulsion system. Recently, the ROSA experiment [33] has shown that solar panel deployment can be completed in a few minutes. Moreover, as an alternative option for power supply, radioisotope electric propulsion (REP) is gaining increasing attention, especially for space missions toward the outer planets. NASA already developed and qualified an advanced Stirling radioisotope generator (ASRG) engineering unit [34]. Moreover, in a broader context, the Joint Radioisotope Electric Propulsion Studies (JREPS) project [35] has recently investigated REP, with the final purpose of designing and testing different technological configurations.

In conclusion, thorough tradeoff analysis is certainly needed to identify the most convenient technological solution for power supply (either SEP or REP), in terms of technological reliability and available payload mass.

7. Concluding remarks

Several types of orbit injection maneuvers were used in past missions to Mars, including long-duration, multiple aerobraking passes, aimed at selecting the desired operational orbit. This research proposes a new strategy for Mars orbit injection, based on aerocapture and low-thrust nonlinear orbit control. The range of altitudes that allow aerocapture are identified as a function of the hyperbolic excess velocity at Mars arrival and ballistic coefficients of the space vehicle, with reference to a large variety of atmospheric density profiles. This preliminary analysis demonstrates that a safe periares altitudinal range leading to aerocapture in all atmospheric conditions does not exist. This result is further confirmed through Monte Carlo simulations, assuming stochastic – yet realistic – atmospheric density profiles. This circumstance implies the need of designing suitable correction maneuvers, aimed at avoiding both impact and escape. Three such types of maneuvers are identified, by minimizing the velocity changes required to achieve aerocapture. However, sufficiently accurate information on atmospheric density and precise selection of the initial flight-path angle lead to avoiding or considerably reducing the need of correction maneuvers. At the end of the first phase, i.e. atmospheric pass, the spacecraft orbit exhibits large dispersions in terms of orbit elements. Therefore, the identification of an effective autonomous guidance strategy, capable of driving the spacecraft toward the desired operational orbit, is mandatory. To do this, low-thrust nonlinear orbit control is proposed as an effective option. A feedback law for the low-thrust direction and magnitude, with saturation on the thrust magnitude, is defined, and is proven to enjoy global stability properties, using the Lyapunov direct method and the LaSalle invariance principle. As a result, the spacecraft travels toward the operational orbit of interest, i.e. either (a) a quasi-synchronous inclined orbit, (b) an areostationary orbit, or (c) a low-altitude, sunsynchronous orbit. Monte Carlo simulations, with stochastic density profiles, point out that the overall propellant budget is considerably reduced, in comparison to direct orbit injection based on chemical propulsion. The overall time of flight typically ranges from 45 to 140 days, and therefore it is much shorter than that required with the use of aerobraking. Furthermore, low-thrust nonlinear orbit control allows the achievement of a variety of operational orbits, with great accuracy. Propellant consumption, time of flight, and reachable orbits represent unequivocal advantages with respect to alternative options, and make the strategy based on aerocapture and low-thrust nonlinear orbit control particularly attractive and convenient for Mars orbit injection.

Declaration of competing interest

The authors declare that they have no known competing financial interests or personal relationships that could have appeared to influence the work reported in this paper.

References

[1] T.W. Finch, Aerodynamic braking trajectories for Mars orbit attainment, J. Spacecraft Rockets 2 (No. 4) (1965) 497–500.
[2] E.M. Repic, M.G. Boobar, F.G. Chapel, Aerobraking as a potential planetary capture mode, J. Spacecraft Rockets 5 (No. 8) (1968) 921–926.
[3] J.R. French, M.I. Cruz, Aerobraking and aerocapture for planetary missions, Aeronaut. Astronaut. 18 (No. 2) (1980) 48–55.
[4] K.D. Mease, R.J. Weidner, J.A. Kechichian, L.J. Wood, M.I. Cruz, Aerocapture – guidance, navigation, and control, in: AIAA Atmospheric Flight Mechanics Conference, 1982. San Diego, CA.
[5] G.D. Walberg, A survey of aeroassisted orbit transfer, J. Spacecraft Rockets 22 (No. 1) (1985) 3–18.
[6] D.P. Fuhry, "A Design Study of Onboard Navigation and Guidance during Aerocapture at Mars," NASA-CR-172053, 1988.
[7] T. J. Brand, D. P. Fuhry, and S. W. Shepperd, "An Onboard Navigation System Which Fulfills Mars Aerocapture Guidance Requirements," paper AIAA-1989-629.
[8] A.J. Calise, "Analytical Guidance Law Development for Aerocapture at Mars," NASA-CR-190615, 1992.
[9] R.W. Powell, R.D. Braun, Six-Degree-of-Freedom guidance and control analysis of Mars aerocapture, J. Guid. Control Dynam. 16 (No. 6) (1993) 1038–1044.
[10] P.F. Wercinski, J.E. Lyne, Mars aerocapture – extension and refinement, J. Spacecraft Rockets 31 (No. 4) (1994) 703–705.
[11] N.X. Vinh, W.R. Wyatt, J.M. Longuski, Mars aerocapture using bank modulation, in: Astrodynamics Specialist Conference, paper AIAA-2000-4424, Denver, CO, 2000.
[12] M. Kumar, A. Tewari, Trajectory and attitude simulation for aerocapture and aerobraking, J. Spacecraft Rockets 42 (No. 4) (2005) 684–693.
[13] M. Kumar, A. Tewari, Trajectory and attitude simulation for Mars aerocapture and aerobraking, J. Spacecraft Rockets 43 (No. 3) (2006) 585–593.
[14] C.R. Heidrich, M.J. Holzinger, R.D. Braun, Optimal information filtering for robust aerocapture generation and guidance, J. Spacecraft Rockets 59 (No. 2) (2021) 524–537.
[15] S.W. Albert, H. Schaub, R.D. Braun, Flight mechanics feasibility assessment for Co-delivery of direct-entry probe and aerocapture orbiter, J. Spacecraft Rockets 59 (No. 1) (2021) 19–32.
[16] E. Roelke, R.D. Braun, Discrete-event drag-modulated guidance performance for venus aerocapture, J. Spacecraft Rockets 58 (No. 1) (2021) 190–199.
[17] M. Pontani, P. Teofilatto, Post-aerocapture orbit selection and maintenance for the aerofast mission to Mars, Acta Astronaut. 79 (2012) 168–178.
[18] J.E. Prussing, B.A. Conway, Orbital Mechanics, Oxford University Press, New York, NY, 2013, pp. 46–54, 197—205.
[19] H. Schaub, J.L. Junkins, Analytical Mechanics of Space Systems, AIAA Education Series, Reston, VA, 2003, pp. 519–525.
[20] R.A. Broucke, P.J. Cefola, On the equinoctial orbit elements, Celestial Mech. 5 (1972) 303–310.
[21] A. Genova, S. Goossens, F.G. Lemoine, E. Mazarico, G.A. Neumann, D.E. Smith, M. T. Zuber, Seasonal and static gravity field of Mars from MGS, Mars Odyssey and MRO radio science, Icarus 272 (2016) 228–245.
[22] R.H. Battin, An introduction to the mathematics and methods of astrodynamics, in: AIAA Education Series, AIAA, New York, 1987, pp. 448–450, 490—494, 529—530, 1987.
[23] S. Giorgi, "Una Formulazione Caratteristica del Metodo di Encke in Vista dell'Applicazione Numerica," Scuola di Ingegneria Aerospaziale, Sapienza Università di Roma, Rome, Italy, 1964.
[24] H.D. Curtis, Orbital Mechanics for Engineering Students, Elsevier, Kidlington, Oxford, U.K., 2014, pp. 695–715.
[25] E. Millour, F. Forget, A. Spiga, M. Vals, V. Zakharov, L. Montabone, F. Lefèvre, F. Montmessin, J.-Y. Chaufray, M. López-Valverde, F. González-Galindo, S. Lewis, P. Read, M.-C. Desjean, F. Cipriani, The Mars Climate Database (MCD Version 5.3), EGU General Assembly Conference Abstracts, 2019, p. 7153.

[26] F. Forget, F. Hourdin, R. Fournier, C. Hourdin, O. Talagrand, M. Collins, S.R. Lewis, P.L. Read, J.-P. Huot, Improved general circulation models of the Martian atmosphere from the surface to above 80 km, J. Geophys. Res. 104 (E10) (1999) 24155–24176.
[27] G. Isoletta, M. Grassi, E. Fantino, D.T. Sangrà, J.P. Álvarez, Feasibility study of aerocapture at Mars with an innovative deployable heat shield, J. Spacecraft Rockets 58 (No. 6) (2021) 1752–1761.
[28] J.L. Cano, ExoMars mission analysis and design – launch, cruise and arrival analyses, in: 20th International Symposium on Space Flight Dynamics, 2007. Annapolis, MD.
[29] M. Pontani, Simple method to determine globally optimal orbital transfers, J. Guid. Control Dynam. 32 (No. 3) (2009) 899–914.
[30] M. Pontani, M. Pustorino, Nonlinear Earth orbit control using low-thrust propulsion, Acta Astronaut. 179 (2021) 296–310.
[31] S. Sastry, Nonlinear Systems. Analysis, Stability, and Control, Springer, New York, NY, 1999, pp. 182–234.
[32] M. Pontani, M. Pustorino, P. Teofilatto, Mars constellation design and low-thrust deployment using nonlinear orbit control, J. Astronaut. Sci. 69 (2022) 1691–1725.
[33] M.K. Chamberlain, S.H. Kiefer, M. LaPointe, P. LaCorte, On-orbit flight testing of the roll-out solar array, Acta Astronaut. 179 (2021) 407–414.
[34] G.R. Schmidt, D.H. Manzella, H. Kamhawi, T. Kremic, S.R. Oleson, J.W. Dankanich, L.A. Dudzinski, Radioisotope electric propulsion (REP): a near-term approach to nuclear propulsion, Acta Astronaut. 66 (2010) 501–507.
[35] M.O. Khan, R. Amin, J. Ervin, J. Lang, D. Landau, S. Oleson, T. Spilker, N. Strange, Joint Radioisotope Electric Propulsion Studies – Neptune System Explorer, " Proceedings of Nuclear and Emerging Technologies for Space 2011, Albuquerque, NM, 2011.